Journal of Alloys and Compounds 581 (2013) 423–430

Contents lists available at ScienceDirect

Journal of Alloys and Compounds

journal homepage: www.elsevier.com/locate/jalcom

Magnetism of ordered and disordered alloys of $R_2Fe_{14}B$ (R = Nd, Er) type

A.E. Teplykh [a], Yu.G. Chukalkin [a], S. Lee [b], S.G. Bogdanov [a], N.V. Kudrevatykh [c], E.V. Rosenfeld [a], Yu.N. Skryabin [a], Y. Choi [d], A.V. Andreev [e,*], A.N. Pirogov [a,c]

[a] Institute of Metal Physics of Ural Division of Russian Academy Sciences, Ekaterinburg 620990, Russia
[b] HANARO, Korea Atomic Energy Research Institute, Daejeon 305-600, Republic of Korea
[c] Ural Federal University, Ekaterinburg 620083, Russia
[d] Department of Materials Science and Engineering, Dankook University, Cheonan 330-714, Republic of Korea
[e] Institute of Physics, Academy of Sciences, Na Slovance 2, 18221 Prague, Czech Republic

ARTICLE INFO

Article history:
Received 12 June 2013
Received in revised form 12 July 2013
Accepted 15 July 2013
Available online 24 July 2013

Keywords:
Rare-earth transition-metal compounds
Neutron powder diffraction
Neutron irradiation
Amorphous state

ABSTRACT

Magnetic susceptibility, magnetization and neutron diffraction measurements have been performed to study structure and magnetic states of crystalline and amorphous $Nd_2Fe_{14}B$ and $Er_2Fe_{14}B$ alloys. In the crystalline state there exists a large (about 20%) anisotropy of Er-sublattice magnetization. Values of the magnetic anisotropy constant of Er ions and the Er–Fe exchange-coupling parameter were estimated using temperature dependence of the Er- and Fe-sublattice magnetizations. Amorphous state of the samples was obtained by irradiation of fast ($E_{eff} \geqslant 1$ MeV) neutrons with a fluence up to the 1.2×10^{20} n/cm^{-2} at 340 K. It is shown that antiferromagnetic coupling between the rare-earth and iron spins is kept in the amorphous state. Amorphization of the samples is found to result in reduction of the Curie temperature (T_C) by about 200 K and almost total absence of coercivity. We suggest that the strong decrease of T_C is a consequence of enhancement of negative Fe–Fe interactions as a result of dispersion of interatomic distances, which is a characteristic feature of the amorphous state.

1. Introduction

Permanent magnets produced on the base of $Nd_2Fe_{14}B$ compound possess record values of maximal magnetic energy product, $(BH)_{max} \geqslant 470$ kJ m^{-3} [1]. These $(BH)_{max}$ values are achieved due to a large magnetocrystalline anisotropy (MCA) and relatively high spontaneous magnetization of $Nd_2Fe_{14}B$.

Despite of a great technological progress, the coercive field of $Nd_2Fe_{14}B$ magnets ($\mu_0 H_c \approx 1.5$ T) is considerably lower than the anisotropy field, which is about 7 T at room temperature [2]. Our basic understanding of the atomic origins of MCA in these complex structures is limited. One of the reasons for such situation is related to a complexity of MCA constants determination. Usually they are determined from a fitting of calculated field magnetization dependencies to experimental curves, measured along and across an easy magnetization direction. It has been suggested that Nd ions formed two sublattices in the $Nd_2Fe_{14}B$ structure, which possess different anisotropy types [3]. Each of sublattice magnetizations tends to orient along its own easy magnetization direction which results in a canted magnetic structure. In such case the MCA constants can be considered only as some effective parameters describing magnetization curves. The task of determination of the MCA constants becomes still more complicated, when rare-earth- and iron-sublattice magnetizations are oriented in opposite directions as, for example, in $Er_2Fe_{14}B$. Under external magnetic field the Er-sublattice magnetizations are oriented against the field direction that causes a skewing of magnetic moments of the Er ions. Therefore, it is important to develop the methods of determination of the MCA-constants, in which the external magnetic field is not used.

Since specific magnetization of $Nd_2Fe_{14}B$ magnets is noticeably lower than that of metallic iron, there still exists a possibility to increase it. One of the ways of increasing magnetization and coercivity of Nd–Fe–B permanent magnets is the creation an exchange-spring coupled magnet [4], where hard ferromagnet nanograins couple with nano-size grains of magnetically soft ferromagnet, possessing high magnetization. Such composite can have both wider and higher hysteresis loop. At present a relatively large amount of exchange-spring magnets is prepared only by melt spinning with wheel surface speed of tens meters per second. However, there is a grave problem in the technology of such materials – isotropic distribution of the easy directions of the $Nd_2Fe_{14}B$ nanograins which reduces the remanence ratio M_r/M_s (where M_r and M_s are the remanent and saturation magnetizations, respectively) of these magnets. An attempt of improvement of the technology was made in Ref. [5]: authors tried to prepare anisotropic powder from melt-spun alloys by means of crushing its flakes to a small

* Corresponding author. Tel.: +420 221912735.
E-mail address: a.andreev@seznam.cz (A.V. Andreev).

0925-8388/$ - see front matter © 2013 Elsevier B.V. All rights reserved.
http://dx.doi.org/10.1016/j.jallcom.2013.07.103

powder particle size of the $Nd_2Fe_{14}B$ phase. However, they could not obtain a high degree of alignment by applying of external magnetic field.

One can guess [6] that the high degree of alignment is possible to obtain in Nd–Fe–B material in fully amorphous state with successive heat treatment for formation of multi-phase nanograin structure of soft (α-Fe and FeB) and hard ($Nd_2Fe_{14}B$) phases. Synthesis of exchange-spring nanocomposite magnets was also realized by spark erosion [7], hot pressing at 600–800 °C under pressure of 100–200 MPa in vacuum [8] and some other methods.

It is important to search for new ways to amorphize Nd–Fe–B materials, to study their structure state and their magnetic properties in the amorphous state. According to Refs. [9,10], the amorphous Nd–Fe–B materials could be synthesized via severe plastic deformation by torsion. Authors of Ref. [11] reported that they achieved an amorphous state of $Nd_2Fe_{14}B$ magnet using irradiation with high-energy electrons. It should be noted that the conclusion about structure state of these materials has been made on the base of X-ray diffraction data. However, the X-ray radiation penetrates only into thin layer near the grain surface of the $Nd_2Fe_{14}B$ alloys, and therefore, their bulk structure remains unclear. Reliable data on the realization of amorphous state can be obtained only from the neutron-diffraction experiment.

In literature there are numerous studies, devoted to influence of fast neutron [12–14], X-ray, γ-ray [15–17] and electron irradiations [18,19] on properties of the Nd–Fe–B magnets. The aim of these works was to study the radiation resistance of Nd–Fe–B magnets. These permanent magnets are used in a high-energy storage ring of current, third-generation synchrotron light sources and, therefore, are subjected to irradiation by the synchrotron radiation, high-energy bremsstrahlung, and bremsstrahlung-produced neutrons. A fluence attained in previous studies by means of neutron irradiation [12,13] did not exceed 6.1×10^{16} n/cm^2, which resulted in significant remanence losses though was not enough to achieve a fully disordered state of the Nd–Fe–B magnet. Next-generation light sources will exceed present the third-generation sources in terms of brightness, coherence, beam power, and energy of radiation by several orders of magnitude [20]. Hence, it is important to know detailed information about neutron irradiation effects on Nd–Fe–B magnets.

In the present work, the $Nd_2Fe_{14}B$ and $Er_2Fe_{14}B$ alloys (hereinafter NFB and EFB, respectively) have been irradiated by the fluence up to 1.2×10^{20} n/cm^2 and transformed into the amorphous state. We studied the atomic structure state and the magnetic properties of these alloys by means of magnetic measurements and neutron diffraction prior and after the irradiation. Among magnetic properties, we have measured magnetization of R- and Fe-ion sublattices in the above alloys, their coercivity, the MCA constant $\boldsymbol{K}_1$ of Er ions and a function of spin-density distribution in the $Er_2Fe_{14}B$ compound.

2. Experimental

The NFB and EFB ingots were smelt in an induction furnace in quartz crucibles under the atmosphere of high-purity argon in a mass of 50 g. Each ingot has been then treated via melt-spinning procedure. Rapidly quenched NFB and EFB alloys were prepared at the wheel surface velocity $V = 20$ m/s as pieces (flakes) of metallic ribbons 30–50 μm thick, 2–5 mm wide and up to 40 mm long. Flakes were milled into powder to measure the magnetic properties and perform the neutron diffraction experiment.

In order to obtain the amorphous state, the powder NFB and EFB samples were irradiated with fast neutrons ($E_{\text{eff}} \geqslant 1$ MeV) to a fluence 1.2×10^{20} n/cm^2 at temperatures below 340 K using sealed aluminum ampoules placed in the water pool of the IVV-2M reactor.

Magnetic measurements were carried out by means of a vibrating-sample magnetometer over the temperature range 5–400 K in field up to 2 T. The errors in the determination of magnetization and temperature were ±1.5% and ±1 K, respectively.

Neutron powder diffraction (NPD) patterns were recorded on the EFB sample with the HRPD diffractometer on the HANARO reactor (Korea) in the temperature range 9–650 K prior to the melt-spinning procedure. The wave length of incident neutron beam in HRPD diffractometer was $\lambda = 1.835$ Å. When the measurements were performed in a cryostat, the temperature stability was ±0.5 K, and if we used a high temperature device, ±1 K.

The neutron diffraction experiments on the rapidly quenched EFB and NFB samples were carried out prior and after the neutron irradiation with the D-2 and D-3 diffractometers, mounted on the reactor IVV-2M (Zarechny, Russia). The wave lengths λ were 1.805 Å and 2.43 Å, respectively. The NPD patterns were calculated by means of Fullprof software [21].

A vanadium standard has been used to convert intensity (in counts) of scattered neutrons on the amorphous EFB sample to units (in cm^{-2}) of the cross section. Corrections for neutron adsorption and multiple scattering were considered according to [22,23].

3. Experimental results

3.1. Crystalline state

As example, Fig. 1 shows the NPD pattern of the EFB sample, recorded with the HRPD diffractometer at 200 K; NPD patterns measured at other temperatures differ from this one only by intensities of reflections. In the temperature region 10–650 K, the EFB sample possesses the tetragonal $Nd_2Fe_{14}B$-type structure (space group $P4_2/mnm$) as the main phase and contains about 2% of the additional α-Fe phase.

Fig. 2 presents the temperature dependencies of the a and c lattice parameters. At $T > 600$ K experimental values of the a and c parameters are taken from Ref. [24]. Above T_C, the thermal expansion has only a phonon contribution from the lattice and its temperature dependence is practically linear. Below T_C, the thermal expansion becomes nonlinear because of a contribution from a spontaneous magnetostriction. We extrapolated the $a(T)$, and $c(T)$ dependencies below T_C using Debye approximation and assuming that the Debye temperature is equal to 450 K as it is pointed in [25]. These dependencies are shown in Fig. 2 by dashed lines. As one can see from comparison of experimental data and calculated lines, the EFB sample exhibits a large spontaneous magnetostriction at low temperatures, $\Delta V/V(10\text{ K}) = 2.4\%$. Our results are in good agreement with previous studies [25–27]. Nevertheless, it is worth to note that we observed an additional anomaly like a jump on the $a(T)$ and $c(T)$ dependencies at $T_{LP} = 298$ K (see insert in Fig. 2).

In the $Nd_2Fe_{14}B$-type structure the Er ions occupy two (4f and 4g) positions, while the Fe atoms are located at five (4c, 4e, 8j, 16k_1 и 16k_2) sites and the B atoms form only one (4g) sublattice

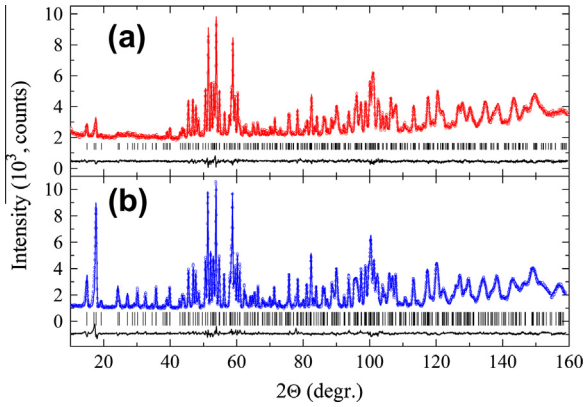

Fig. 1. Observed (circles) and calculated (solid lines) neutron powder diffraction patterns of the crystalline $Er_2Fe_{14}B$ sample at (a) 600 K and (b) 200 K. Vertical bars indicate the positions of nuclear and magnetic Bragg reflections. Difference between the observed and calculated intensities is given at the bottom of the patterns.

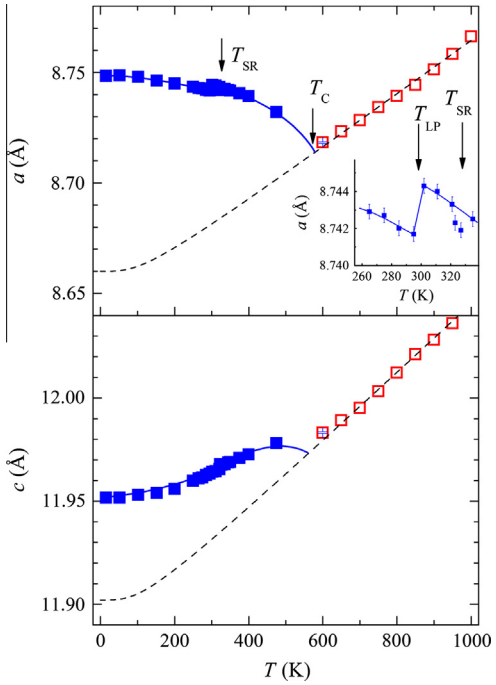

Fig. 2. Temperature evolution of the *a* and *c* lattice parameters of the crystalline $Er_2Fe_{14}B$ sample. The arrow point to the temperature of the spin-reorientation transition (T_{SR}), Curie temperature (T_C) and the temperature of jump on $a(T)$ and $c(T)$ dependencies (T_{LP}). The dashed lines represent extrapolation of the paramagnetic behavior onto the magnetically ordered range.

(see Table 1). A refinement of crystal structure parameters at 600 K (see Fig. 1b) results in the Fe-deficit composition of the EFB sample, which is determined as $Er_2Fe_{13.8}B$.

Magnetic structure of the EFB is described by the wave vector **k** = 0 over whole temperature region. The Er- and Fe-sublattice magnetizations are mutually antiparallel within the error (±10°) of a determination of magnetization directions. In our calculations we supposed that magnetizations of the Er ions at the 4*f* and 4*g* positions were the same, and the Fe-ion moments at the 4*c*, 4e, 8*j*, 16k_1 и 16k_2 sites were assumed independent on the crystallographic positions. Magnetic moments of all the Er and Fe sublattices are oriented parallel to the basal plane at temperatures below 325 K and they are arranged along the *c*-axis at temperatures above 327 K, so, the spontaneous spin-reorientation transition (SRT) takes place between these temperatures. This is the first order transition of the "easy plane–easy axis" type. Therefore, we considered that in our EFB sample the Er- and Fe-sublattice magnetizations are rotated from the basal plane to the *c*-axis at the T_{SR} = 326 K. According to study of the specific heat [28] the SRT occurs at 323 K in the EFB single crystal, in good agreement with our results. The SRT becomes apparent on the temperature dependency of the Er-ion magnetization ($\mu_{Er}(T)$) as a jump at the T_{SR} (see Fig. 3). One can see from Fig. 3 that the μ_{Er} value decreases by about $\Delta\mu_{Er}$ = 0.8 μ_B in the SRT region, so, the anisotropy of Er-ion magnetization is $\Delta\mu_{Er}/\mu_{Er}$ (327 K) ≈ 20%. In comparison with the $\mu_{Er}(T)$ dependence the temperature evolution of the Fe-ion magnetization ($\mu_{Fe}(T)$) is rather smooth (see Fig. 3).

It would be tempting to relate the SRT with the jumps on $a(T)$ and $c(T)$ dependencies at T_{LP} = 298 K (see insert in Fig. 2). But, we cannot explain the difference in 28 K between the T_{SR} and T_{LP}.

To make unambiguous decision about the change of the crystal structure and magnetic states in the result of a fast neutron irradiation, we measured NPD patterns of the rapidly quenched EFB sample with the D-2 diffractometer before and after irradiation. This diffractometer was also used for recoding NPD patterns obtained prior and after neutron irradiation of the rapidly quenched NFB sample. The NPD patterns of non-irradiated samples are presented in Figs. 4a and 5a; calculated lines have been obtained with parameters, which are given in Table 1. Both samples contain the crystalline $Nd_2Fe_{14}B$-type phase as the main phase, whereas content of the amorphous phase does not exceed 10% in each sample. It is worth to note that prior irradiation the content of the α-Fe phase was about 7% in the NFB sample.

Table 1
Lattice constants *a*, *b*, *c* and volume of unit cell *V*, coordinates of positions (space group $P4_2/mnm$), the average Nd-, Er- and Fe-ion magnetic moments μ_z^{Nd}, μ_x^{Er} and μ_z^{Fe}, contents of the $Nd_2Fe_{14}B$ and α-Fe phases, agreement factor and χ^2 for the $Nd_{12}Fe_{82}B_6$ and $Er_2Fe_{14}B$ samples at room temperature.

Structural parameter	$Nd_2Fe_{14}B$	$Er_2Fe_{14}B$
a, *b* (Å)	8.816(1)	8.744(1)
c (Å)	12.240(2)	11.968(2)
V (Å^3)	951.4(2)	914.3(5)
R, 4*f*: *x*	0.267(1)	0.273(1)
R, 4g: *x*	0.142(1)	0.147(1)
Fe, 4*e*: *z*	0.113(1)	0.112(1)
Fe, 8j_1: *x*	0.098(1)	0.097(1)
z	0.204(1)	0.201(1)
Fe, 8j_2: *x*	0.318(1)	0.318(1)
z	0.246(1)	0.249(1)
Fe, 16k_1: *x*	0.224(1)	0.222(1)
y	0.567(1)	0.567(1)
z	0.128(1)	0.127(1)
Fe, 16k_2: *x*	0.037(1)	0.036(1)
y	0.361(1)	0.360(1)
z	0.176(1)	0.170(1)
B, 4g: *x*	0.625(2)	0.636(2)
μ_z^{Nd} (μ_B)	1.5(1)	
μ_z^{Fe} (μ_B)	1.9(1)	
μ_x^{Er} (μ_B)		4.1(1)
μ_x^{Fe} (μ_B)		−1.9(1)
$Nd_2Fe_{14}B$, mass%	93.0(5)	98.0(2)
α-Fe, mass%	7.0(5)	2.0(2)
R_{Bragg} (%)	3.19	5.53
χ^2	4.50	4.46

3.2. Amorphous state

Figs. 4b and 5b show NPD patterns of the NFB and EFB samples after irradiation with fast neutrons up a fluence of 1.2 × 10^{20} n/cm^2. Both patterns include narrow half-width peaks at angles 2θ = 53°,

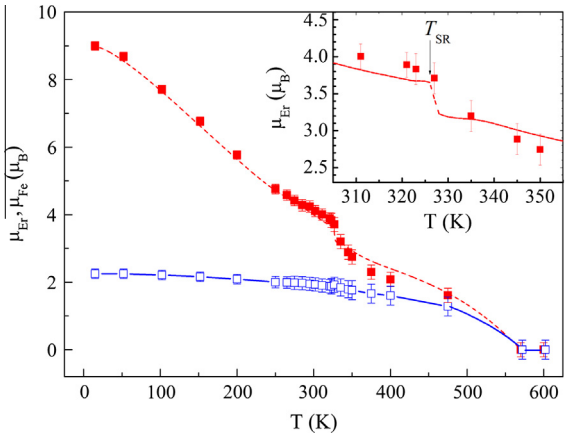

Fig. 3. Temperature dependencies of Er- and Fe-sublattice magnetizations for the crystalline $Er_2Fe_{14}B$ sample. The dashed line is calculation (see text). The jump of Er-sublattice magnetization is shown in the insert. The arrow (T_{SR}) points to the temperature of the spin-reorientation transition.

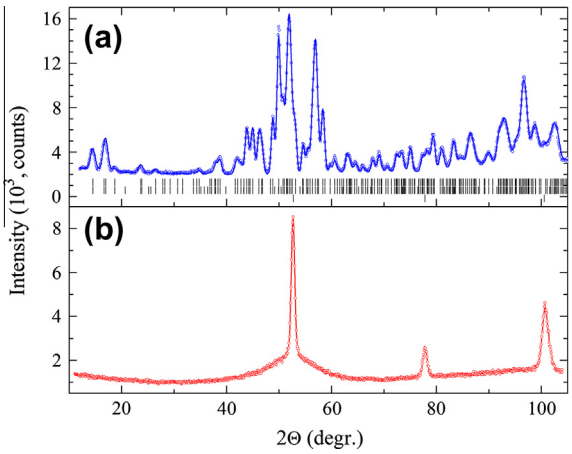

Fig. 4. Neutron diffraction patterns of the $Nd_{12}Fe_{82}B_6$ sample at room temperature before (a) and after (b) neutron irradiation.

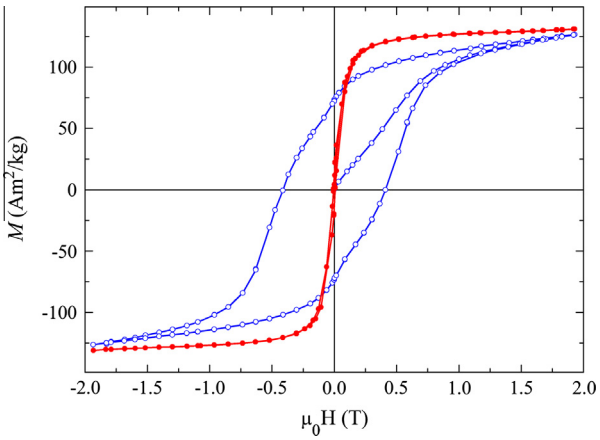

Fig. 6. Magnetization curves of the $Nd_{12}Fe_{82}B_6$ sample at room temperature before (open circles) and after (filled circles) neutron irradiation.

78° and 101° and also wide maximum at $2\theta = 53°$. The narrow peaks are originated from neutron scattering on the α-Fe lattice, and the wide maximum is evidence of that we have achieved the amorphous state of the $Nd_2Fe_{14}B$ phase in both samples.

Fig. 6 presents magnetization curves and hysteresis loop for the NFB sample at room temperature before and after irradiation, i.e., in crystalline and amorphous states. One can see that the magnetization at the field $\mu_0H = 2$ T is almost the same in both states, but, a coercitivity decreases noticeably in the amorphous state. Magnetization curves are changed substantially in the low-field region.

Fig. 7 shows experimental temperature dependence of the magnetization of the amorphous NFB sample below $T = 300$ K at the field $\mu_0H = 1$ T. We extrapolated this dependence to higher temperatures using the Stoner's law $M(T) = M(0)\,(1 - (T/T_C)^2)^{1/2}$ and estimated the T_C in the amorphous state as $T_C \approx 450$ K, this is by about 150 K lower than T_C in the crystalline state.

Fig. 8 presents the magnetization curves for the EFB sample in the crystalline and amorphous states at room temperature. It is seen that the amorphization of the sample is accompanied by the lowering of the magnetization by two times in comparison with that in the crystalline state. The coercitivity is very small in the amorphous state.

Fig. 9 shows temperature dependence of the magnetization of the amorphous EFB sample when it was cooled at zero field and at various fields up to 0.7 T. As one can see, a sudden change of the magnetization takes place at about $T_f \approx 70$ K at the minimal field. Below this temperature the magnetization irreversibility is observed: the field-cooled magnetization curve and the zero-field cooled one are different. The T_f value decreases with increasing field and the anomaly disappears at $\mu_0H = 0.7$ T. Such magnetization behavior is a typical for the systems with competitive exchange interactions in reentrant spin glass state [29]. At the same time the sample possesses a spontaneous magnetization. Therefore, the sample shows properties, which are characteristic for the ferrimagnets and spin glass systems, so we may classify such magnetic state as the mixed state.

Fig. 10 presents temperature dependence of the magnetization of the amorphous EFB sample at $\mu_0H = 1$ T. T_C of the sample was measured at the low field, $\mu_0H = 5$ mT. We determined the T_C to be equal to 314(2) K, which is noticeably lower that in the crystalline sample. According to our AC-susceptibility measurements the T_C value of crystalline sample was 570(1) K. Thus, the amorphization of the EFB sample results in reduction of T_C by ~250 K, this is the reason, why the magnetization of the amorphous sample is much lower that of crystalline one at room temperature.

To find a saturation magnetization of the EFB sample we extrapolated a high field part of $M(H)$ dependencies to the infinite magnetic field making $M = f(1/H^2)$ plots. Using such extrapolation results and taking into account the amount of α-Fe phase, we calculated the magnetic moments of the formula unit for the EFB sample in crystalline and amorphous states (M_{cr} and M_{am}, respectively) at 5 K. Following values were obtained: $M_{cr} = 10.7\ \mu_B$ and $M_{am} = 10.1\ \mu_B$. The obtained M_{cr} value agrees well with $\mu_{f.u}$, deter-

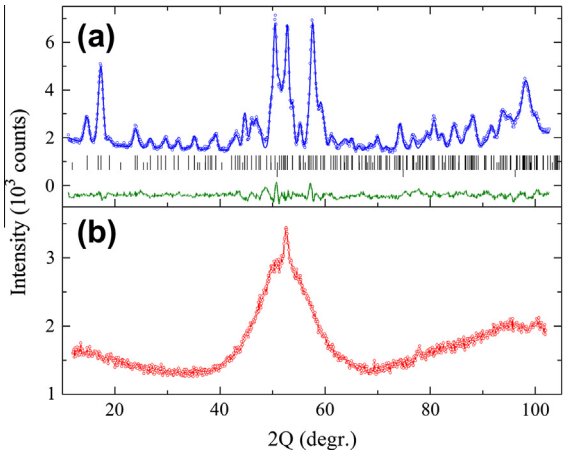

Fig. 5. Neutron diffraction patterns of the $Er_2Fe_{14}B$ sample at room temperature before (a) and after (b) neutron irradiation.

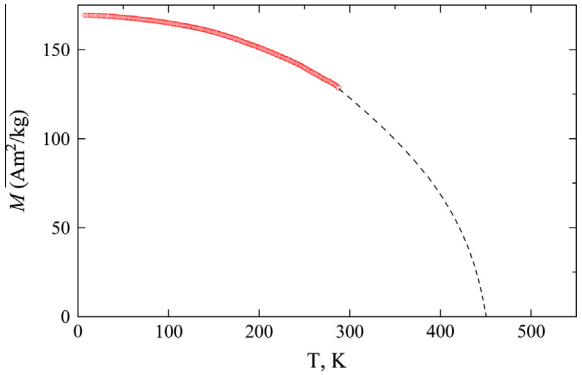

Fig. 7. Temperature dependence of the magnetization of the amorphous $Nd_{12}Fe_{82}B_6$ sample. Points are experiment, dashed line is the extrapolation.

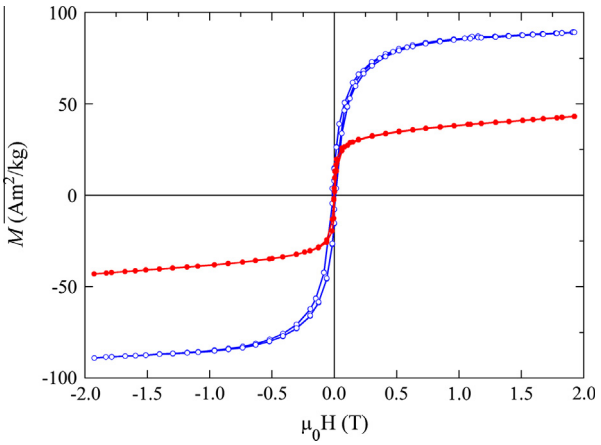

Fig. 8. Magnetization curves of the $Er_2Fe_{14}B$ sample at room temperature before (open circles) and after (filled circles) neutron irradiation.

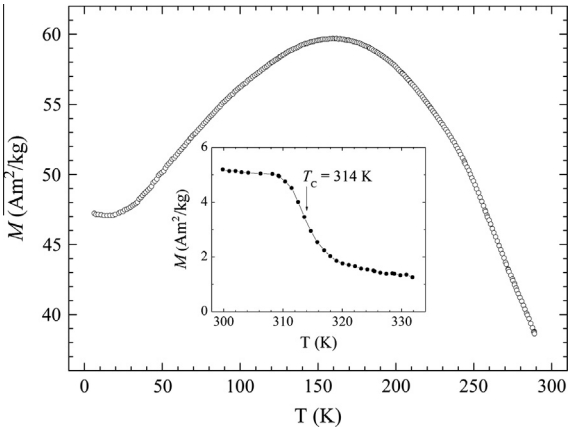

Fig. 10. Temperature evolution of the magnetization of the amorphous $Er_2Fe_{14}B$ sample at the field $\mu_0H = 1$ T. The insert shows temperature dependence of the magnetization at $\mu_0H = 5$ mT.

mined above from the neutron diffraction data of the crystalline sample. Close values of the M_{cr} and M_{am} allow to make the conclusion that the ferrimagnetic character of Er- and Fe-ion-moment ordering is kept in the amorphous sample though the Er and Fe sublattices are absent in the crystallographic sense. This conclusion is corroborated by the presence of the maximum on the $M_{am}(T)$ dependence at ~150 K. This maximum is the result of a strong decreasing of the Er-ion magnetization and comparatively slow falling of the Fe magnetization with temperature. The difference in the temperature dependencies of the Er- and Fe-ion magnetizations causes a maximum on the resulting $M_{cr}(T)$ curve, when the Er- and Fe-ion magnetizations are coupled by antiferromagnetic exchange interaction. A slow fall of the Fe-ion magnetization with temperature is explained by an existence of a strong Fe–Fe interaction in $R_2Fe_{14}B$ compounds [1,2].

4. Discussion

4.1. Crystalline state of the EFB sample

As was noted in Introduction, a widespread method of determination of the MCA constants is description of the magnetization curves, measured along and across the easy magnetization direction in the case of uniaxial crystals. But the difficulties emerge if this method is applied to highly anisotropic magnetic materials with more than one sublattice: deformation of the magnetic structure occurs by application of high magnetic fields. Therefore, methods in which high magnetic fields are not used have irrefutable advantages. By now several models are suggested [30,31], which allow estimating the MCA constants in $R_2Fe_{14}B$ materials. In general outline the same idea underlies in all models: the rare-earth and iron sublattices are described by own MCA constants and their sum determines total anisotropy energy of a magnet. A difference between models concerns mainly a procedure of Hamiltonian minimalizing. In our model the angle between the *c*-axis and the Fe-sublattice magnetization (θ_{Fe}) is an independent parameter while the angle between the *c*-axis and the Er-sublattice magnetization (θ_{Er}) should be found by Hamiltonian minimalizing.

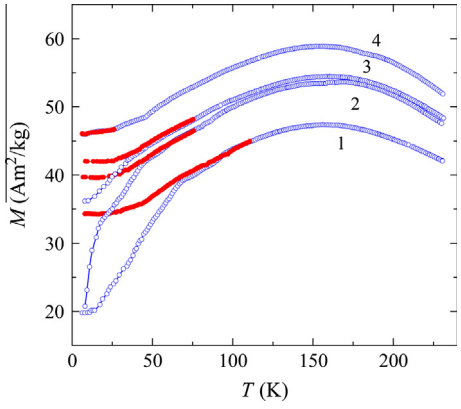

Fig. 9. Temperature dependence of the magnetization of the amorphous $Er_2Fe_{14}B$ sample cooled at zero field (open circles) and at various fields (filled circles): 1 – $\mu_0H = 0.085$ T, 2–0.21 T, 3–0.4 T, 4–0.7 T.

In order to obtain the MCA constants and the parameter Er–Fe exchange interaction in the EFB sample we write Hamiltonian in following view:

$$H_R = (g_J - 1)\cdot I_{ErFe}\cdot(J_{f_z} + J_{g_z})\cos(\theta_{Fe}) + [\cos(\theta_{Er})(J_{f_x} + J_{g_x}) + \sin(\theta_{Er})(J_{f_y} + J_{g_y})]\sin(\theta_{Fe}) + k_1^f\cdot J_{f_z}^2 + k_2^f\cdot J_{f_z}^4 + k_1^g\cdot J_{g_z}^2 + k_2^g\cdot J_{g_z}^4 - g_J\mu_B H(J_f + J_g + K_{Fe}\cos(\theta_{Fe})^2 - (\mu_{Fe}H), \quad (1)$$

where g_J is the Landé factor; I_{ErFe} is the parameter of Er–Fe exchange interaction; $\vec{J}$ is the operator of a full mechanical moment of the Er ion; J_{fx}, J_{fy}, J_{fz}, J_{gx}, J_{gy} and J_{gz} are the projections of $\vec{J}$ of the Er ions at the 4*f* and 4*g* positions to the *x*, *y* and *z* axes; k_1^f, k_2^f, k_1^g and k_2^g are the first and second microscopic MCA constants of the Er ions at the 4*f* and 4*g* positions. We assumed that $k_1^f = k_1^g = k_1$, and $k_2^f = k_2^g = k_2$. Calculation curve describing the experimental $\mu_{Er}(T)$ dependence is presented in Fig. 3 by the dashed line. At minimalization procedure we obtained values of the I_{ErFe} parameter and the first and second microscopic MCA constants for the Er ions at the 4*f* and 4*g* positions, which are given in Table 2. Information about I_{ErFe}, k_1 and k_2 allows us to estimate energies of the Er–Fe exchange and magnetic anisotropy by means of following equations:

$$K_1^{Er} = N_{Er}k_1\cdot J\cdot(J - 1/2), \quad (2)$$

$$E_{ErFe} = I_{ErFe}\cdot J, \quad (3)$$

Table 2
The microscopic (k_1^{Er}, k_2^{Er}) and macroscopic (K_1^{Er}, K_2^{Er}) MCA constants of the Er ions. The parameter (I_{Er-Fe}) and energy (E_{Er-Fe}) of the Er–Fe exchange coupling.

I_{Er-Fe} (J/kg)	E_{Er-Fe} (J/kg)	k_1^{Er} (J/kg)	k_2^{Er} (J/kg)	K_1^{Er} (J/kg)	K_2^{Er} (J/kg)
2.2×10^3	1.6×10^4	−26	0.6	−1390	3

where N_{Er} is number of the Er ions per cubic meter. The values of K_1^{Er} and E_{ErFe} are given in Table 2. As one can see, these energies are close in their values. This factor causes the large magnetization anisotropy of the Er ions at the SRT. The obtained values of K_1^{Er} and E_{ErFe} agree with those found in [32] but differ from values presented in [33].

5. Amorphous state of the EFB sample

The NPD patterns of the EFB amorphous sample have been recorded at $T = 6$, 150, 295 and 360 K. The NPD patterns measured at $T = 6$ K (below T_C) and 360 K (above T_C) are presented in Fig. 11 as example. It is seen that the pattern at 6 K differs from that obtained at 360 K and this difference arises from a magnetic scattering. It is worthy to note the intensive small angle neutron scattering (see inset in Fig. 11), which is absent in the crystalline sample. The magnetic scattering at 360 K originates may be from ferromagnetic correlations which exist in paramagnetic region close to T_C. Using Guinier asymptotic we found that the length of the correlations is about 8–15 Å. The presence of the small angle scattering at 6 K in the interval $q = 2\pi \sin\theta/\lambda = 0.08$–$0.18$ Å^{-1} is the evidence of existence of the magnetic fluctuations in the ferrimagnetic amorphous sample. These fluctuations are fluctuations of the z-projection of the magnetic moments. Apparently, the fluctuations originate from the competition between ferro- and antiferromagnetic exchange interactions in the regions with nanometer scale. Our estimations show the length of these fluctuations is about 20 Å.

Now we try to get a quantitative information from the observed NPD patterns of the EFB amorphous sample. As it is well known, the intensity of unpolarized neutron scattering involves the following main contributions: instrumental background, nuclear (coherent, incoherent and multiple) and magnetic scattering. As it was pointed above, the EFB amorphous sample is paramagnetic at 360 K. In this case the paramagnetic scattering presents in a diffraction pattern. The cross section of this scattering is [34]:

$$d\sigma_p/d\Omega = 2/3(r_0\gamma)^2[c_{Fe}s_{Fe}(s_{Fe}+1)f_{Fe}^2(q) + c_{Er}s_{Er}(s_{Er}+1)f_{Er}^2(q)], \quad (4)$$

where r_0 is the classical radius of the electron; γ is the magnetic moment of the neutron; c_{Fe}, c_{Er} are the Fe-atom and Er-ion concentrations in the sample, respectively; s_{Fe} and s_{Er} – the effective spin-quantum numbers of the Fe atoms and Er ions, respectively, (we consider $s_{Er} = g_J J/2$); $f_{Fe}(q)$ and $f_{Er}(q)$ are the magnetic form-factors of the Fe atoms and Er ions, respectively; $q = 4\pi \sin(\theta/\lambda)$ is the vector scattering. The temperature decrease below T_C results in a modulation of the paramagnetic scattering. If the instrumental background and nuclear scattering do not change visibly with temperature, we can obtain a magnetic contribution to NPD patterns. The pattern obtained in such a way may be used for description of magnetic properties of the amorphous sample.

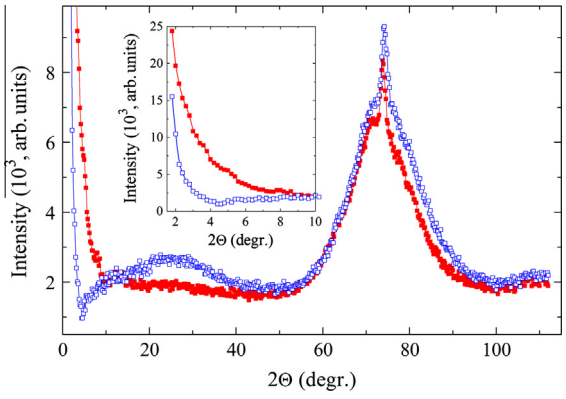

Fig. 11. Neutron diffraction patterns of the $Er_2Fe_{14}B$ amorphous sample at 6 K (open symbols) and 360 K (filled symbols). Small angle parts of the patterns are presented in insert.

We may write the magnetic structure factor for the amorphous state in the form as in [35]:

$$S_M(q) = (d\sigma_M/d\Omega - d\sigma_p/d\Omega)/d\sigma_p/d\Omega, \quad (5)$$

where $d\sigma_M/d\Omega$ is the differential cross section of the magnetic scattering in the magnetically ordering state. Physical sense of Eq. (5) is clear enough: the $S_M(q)$ is the normalized difference of magnetic scattering intensities in the magnetically ordered and the paramagnetic states.

In order to characterize the magnetic ordering in the real space of isotropic amorphous solid state, the so-called function of magnetic distribution is usually used [36]:

$$G_{MA}(r) = 4\pi r[\rho_M(r) - \rho_M^0(r)], \quad (6)$$

where $\rho_M(r) = \rho_{Fe}(r) < \mathbf{s}(0)\mathbf{s}(r) > /s(s+1)$; $\rho_{Fe}(r)$ is the density of the Fe-ion magnetic moments in r-distance from the atom which is taken as the first atom; $\rho_M^0(r)$ is the average value of $\rho_M(r)$. $\rho_M(r)$ may have both positive and negative values in dependence on the orientation of $\boldsymbol{s}(r)$ relative to the spin of the first atom. In such an approach, the veritable three-dimensional distribution of spins is replaced by the one-dimensional arrangement. The $G_{MA}(r)$ function can be expressed by the $S_M(q)$ factor in following view (see, for example, [35]):

$$G_{MA}(r) = 2/\pi \int_0^{q_{max}} qS_M(q)\Phi(q)sin(qr)dq, \quad (7)$$

where $\Phi(q)$ is the modified function which reduces influence of breaking off the integration by q at the q_{max} achievable in the experiment. The q_{max} equals to be about 5 Å^{-1} because the $f(q)$ form-factor falls fast with q. We choose the $\Phi(q)$ function as $\Phi(q) = f^2(q)$. In the experiment it is more convenient to use the other function instead of the $S_M(q)$ factor:

$$S_{M1}(q) = f^2(q)S_M(q) \equiv \Phi(q)S_M(q), \quad (8)$$

since determination of $S_{M1}(q)$ does not demand information about an explicit view of the $f(q)$ form-factor. We found the $S_{M1}(q)$ function by following equation:

$$S_{M1}(q) = [J_{6K} - J_{360K}/D(q)]/(2/3)(r_0\gamma)^2[c_{Fe}s_{Fe}(s_{Fe}+1) + c_{Er}s_{Er}(s_{Er}+1)], \quad (9)$$

where J_{6K} and J_{360K} are normalized intensities of scattered neutrons at 6 and 360 K, respectively; $D(q)$ is a correction for change of the nuclear intensity with temperature. To reduce the statistical error in the determination of $S_{M1}(q)$ we made averaging-out in three nearest 2θ points. The temperature correction has been taken in the view as Debye–Waller factor: $D = \exp[-2B(\sin\theta/\lambda)^2]$. The value of B was determined from measuring in the high 2θ angle region where the magnetic scattering is practically absent. An increase in B by 0.35 Å^2 is obtained when the temperature increases from 6 to 360 K. Correction for the thermal expansion has been carried out too, for that we used the temperature dependence of angle position of the (1 1 0) reflection resulting from α-Fe (see Fig. 5b). In the same manner we obtained the $S_{M1}(q)$ factor at 150 K. Unfortunately, we did not succeed in determination of $S_{M1}(q)$ at 295 K because the magnetic contribution in the NPD pattern at 295 K was low and comparable with a statistical error.

Thus, we obtained the $S_{M1}(q)$ values for the amorphous EFB sample. They are presented in Fig. 12a. The $S_{M1}(q)$ maxima decrease appreciably with increasing temperature from 6 K up to 150 K. Calculated arbitrary intensity of the magnetic scattering at

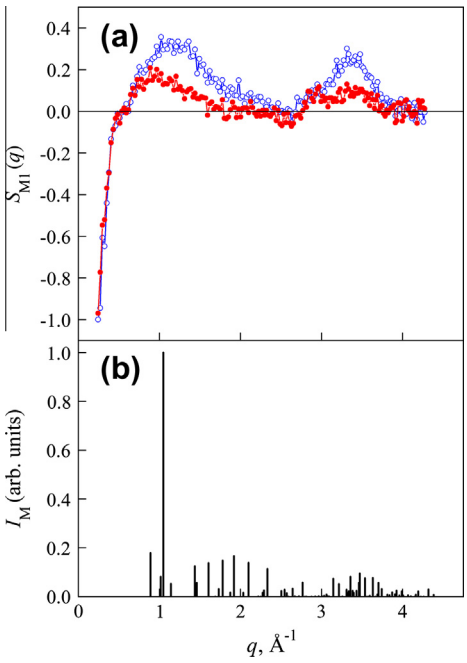

Fig. 12. (a) Magnetic structure factor for amorphous $Er_2Fe_{14}B$ sample at 6 K (open symbols) and 150 K (filled symbols). (b) Intensity of magnetic scattering on the crystalline $Er_2Fe_{14}B$ sample at 6 K.

6 K is shown for the crystalline sample in Fig. 12b for comparison. It is seen that $S_{M1}(q)$ maxima are located at about the same q values as magnetic Bragg reflections for the crystalline sample. This means that the main character of the magnetic structure is kept in the amorphous state.

Results of numerical integration of Eq. (7) are presented in Fig. 13 which shows the $G_{MA}(r)$ function at 6 and 150 K. The $G_{MA}(r)$ function gives information about the space distribution the magnetic atoms and the magnetic moment orientations in the amorphous sample. As can be seen from Fig. 13, the distinct maxima are located in the positive region at $r_0 = 0.53$ Å, $r_1 = 2.26$ Å, and a maximum (in absolute value) is situated in the negative field at $r_2 = 3.25$ Å. Positive maxima point to predominantly ferromagnetic orientation of moments in the distance r from the first atom. Negative maxima indicate the antiferromagnetic arrangement of moments. The $G_{MA}(r)$ maximum at r_0 is originated apparently from a distribution of magneto-active electrons around the first atom.

Let us compare the $G_{MA}(r)$ function of the amorphous sample with the picture of the magnetic structure of the crystalline EFB

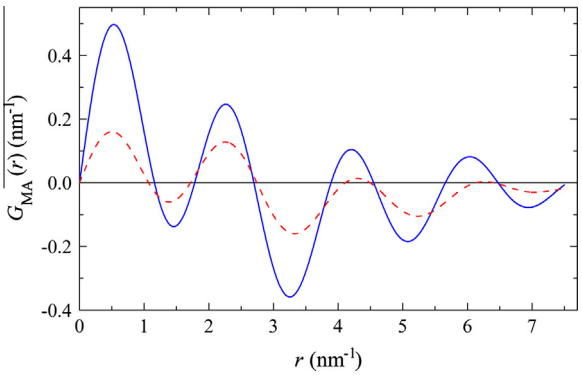

Fig. 13. Correlation function $G_{MA}(r)$ for the amorphous $Er_2Fe_{14}B$ sample at 6 K (solid line) and 150 K (dashed line).

specimen. As was shown above, in the crystalline EFB sample the Fe atoms occupy six crystallographic positions and the Er ions are located at two sites. Distances between Fe atoms change from 2.32 to 2.75 Å while the Fe atoms and Er atoms are positioned from each other at distances between 2.99 до 3.39 Å depending on the Fe (Er) atom positions. Taking into account the multiplicity of the positions, we calculated the average weighted distances between the Fe atoms as $\langle r_{Fe-Fe}\rangle = 2.54$ Å and between the Fe atoms and Er ions as $\langle r_{Fe-Er}\rangle = 3.18$ Å. These values are close to pointed above distances $r_1 = 2.26$ Å and $r_2 = 3.25$ Å, at which the negative and positive $G_{MA}(r)$ maxima are located. In the EFB crystal the Fe-atom moments are coupled ferromagnetically, whereas, the Fe-atom and Er-ion moments are oriented antiferromagnetically. Therefore, positive maxima at r_1 and negative maxima at r_2 agree with ferromagnetic and ferrimagnetic arrangements of the Fe–Fe- and Fe–Er- moments at 6 K. Thus, the ferrimagnetic character of magnetic ordering is kept in the amorphous sample though the translation symmetry is absent. When the temperature increases, atomic vibrations increase and destroy the magnetic arrangement that results in the lowering of the intensity of the $G_{MA}(r)$ maxima at 150 K.

6. Conclusions

The structural state and magnetic properties of the crystalline and amorphous NFB and EFB samples have been studied by means of neutron diffraction and magnetic measurements. Amorphous state of the NFB and EFB samples was produced by the fast ($E_{eff} \geqslant 1$ MeV) neutron irradiation up to 1.2×10^{20} n/см^2 fluence.

The evaluation of the Er-sublattice magnetization temperature behavior shows the distinct ($\Delta\mu_{Er}/\mu_{Er}(320\ K) \approx 20\%$) dependence of the magnetization value on its orientation in the crystal.

Using neutron diffraction data and our model, we estimated the values of the MCA constant of the Er-sublattice and the parameter of the Er–Fe exchange interaction. The energy of the Er-sublattice magnetic anisotropy is closed to the Er–Fe exchange interaction energy that causes the clear magnetization anisotropy effect at the spin-reorientation transition.

The amorphization of the NFB and EFB samples results in strong decrease of T_C and almost total collapse of coercivity.

For the EFB amorphous sample the magnetic structure factors are calculated from the NPD patterns, obtained at 6 and 150 K. The magnetic distribution function is reestablished by means of Fourier transform from neutron data. This function characterizes a space distribution of magnetic atoms and mutual orientations of their magnetic moments in the amorphous EFB sample.

A local magnetic ordering in the EFB amorphous sample is similar in general to the ferrimagnetic structure in the crystalline specimen. However, the magnetization anomalies are observed in low temperature region, that it is typical for the reentrant transition in spin glasses. These anomalies originate, on our opinion, from the fluctuations of z-projection of the magnetic moments. Existence of the fluctuations is the sequence of a competition of positive and negative interactions between the Fe atoms.

Acknowledgements

The work was done within RAS Program (Project No. 01.2.006 13394) and with partial support of Projects 12-02-12065-DBR_M, "Quant mesoscopic and disordered structures" of UD of RAS Nos. 12-П-2-1019 and 12-П-2-1041 and Project of RBRF No. 12-02-00864. One (Y. Choi) of us would like to thank MOST (Grant No. 2012R1A1A4A01014953). A.V.A. thanks support from the Czech Science Foundation (Prant P204/12/0150).

References

[1] E. Burzo, Rep. Prog. Phys. 61 (1998) 1099.
[2] K.H.J. Buschow, Rep. Prog. Phys. 54 (1991) 1123.
[3] D. Haskel, J.C. Lang, Z. Islam, A. Cady, M. van Veenendall, P.C. Canfield, Phys. Rev. Lett. 95 (2005) 217207.
[4] R. Coehoorn, D.B. de Mooij, C. de Waard, J. Magn. Magn. Mater. 80 (1989) 101.
[5] S.V. Andreev, N.V. Kudrevatykh, V.I. Pushkarsky, P.E. Markin, N.K. Zaikov, E.N. Tarasov, J. Magn. Magn. Mater. 187 (1998) 83.
[6] M. Sagawa, in: S. Kobe, P. McGuiness (Eds.), Proceedings of the 21st Workshop on Rare-Earth Permanent Magnets and Their Applications, Ljublyana, 2010, p. 183.
[7] Y.J. Tang, F.T. Parker, H. Harper, A.E. Berkowitz, K. Vecchio, A. Rohatgi, Bao-Min Ma, Appl. Phys. Lett. 86 (2005) 122507.
[8] D. Lee, J.S. Hilton, S. Liu, Y. Zhang, G.C. Hadjipanayis, C.H. Chen, IEEE Trans. Magn. 39 (2003) 2947.
[9] V.S. Gaviko, A.G. Popov, A.S. Ermolenko, K.N. Shchegoleva, V.V. Stolyarov, D.V. Gunderov, Phys. Met. Metallogr. 92 (2001) 158.
[10] A.G. Popov, B.C. Gaviko, N.K. Shchegoleva, L.A. Shreder, V.V. Stolyarov, D.V. Gunderov, Kh.Yu. Zhan, V. Li, L.L. Li, Phys. Met. Metallogr. 104 (2007) 238.
[11] A. Nino, T. Nagase, Y. Umakoshi, Mater. Sci. Eng., A 449–451 (2007) 1115.
[12] J.R. Cost, R.D. Brown, A.L. Giorgi, J.T. Stanley, IEEE Trans. Magn. 24 (1988) 2016.
[13] R.D. Brown, J.R. Cost, IEEE Trans. Magn. 25 (1989) 3117.
[14] R.D. Brown, J.R. Cost, G.P. Meisner, E.G. Brewer, J. Appl. Phys. 64 (1988) 5305.
[15] S. Okuda, K. Ohashi, N. Kobayashi, Nucl. Instr. Methods. B 94 (1994) 227.
[16] H.B. Luna, X.K. Maruyama, N.J. Colella, J.S. Hobbs, R.S. Hornady, B. Kulke, J.V. Palomar, Nucl. Instr. Methods. A 285 (1989) 349.
[17] K. Boockman, M. Liehr, W. Rodewald, E. Salzborn, M. Schlapp, B. Wall, J. Magn. Magn. Mater. 101 (1991) 345.
[18] P. Colomp, T. Oddolaye, P. Ellaeume, Demagnetization of permanent magnets to 180 MeV electron beam, ESRF/MACH/93-09, 1993.
[19] J. Pfluger, G. Heintze, I. Vasserman, Rev. Sci. Instrum. 66 (1995) 1946.
[20] The Advanced Photon Source – a National Synchrotron Radiation Research Facility at Argonne National Laboratory, ANL/APS/TB-25-Rev., Argonne National Laboratory, 1997.
[21] J.C. Rodriguez, Physica B 192 (1993) 55.
[22] K.D. Rouse, M.J. Cooper, E.J. York, A. Chakera, Acta Cryst. A 26 (1970) 682–691.
[23] I.A. Blech, B.L. Averbach, Phys. Rev. 137 (1965) 1113.
[24] H. Fujii, H. Nagata, Y. Uwatoko, T. Okamoto, J. Magn. Magn. Mater. 70 (1987) 331.
[25] A.V. Andreev, in: K.H.J. Buschow (Ed.), Handbook of Magnetic Materials, vol. 8, North-Holland, Amsterdam, 1995, p. 59.
[26] A.V. Andreev, A.V. Deryagin, S.M. Zadvorkin, S.V. Terent'ev, Sov. Phys. Solid State 27 (1985) 987.
[27] N. Yang, K.W. Dennis, R.W. McCallum, M.J. Kramer, Y. Zhang, P.L. Lee, J. Magn. Magn. Mater. 295 (2005) 65.
[28] V. Basso, C.P. Sasso, M. Küpferling, K.P. Skokov, O. Gutfleisch, J. Appl. Phys. 109 (2011) 083910.
[29] T. Yokota, Phys. Rev. B 39 (1989) 523.
[30] M.R. Ibarra, Z. Arnold, P.A. Algarabel, L. Morellon, J. Kamarád, J. Phys. Condens. Matter. 4 (1992) 9721.
[31] A.T. Pędziwiatr, B.F. Bogacz, R. Gargula, Nukleonika 48 (2003) S59.
[32] Y.B. Kim, J. Han-min, J. Magn. Magn. Mater. 222 (2000) 39.
[33] R. Verhoef, P.H. Quang, J.J.M. Franse, R.J. Radwanski, J. Magn. Magn. Mater. 83 (1990) 139.
[34] Yu.A. Izyumov, R.P. Ozerov, Magnetic Neutron Diffraction, Nauka, Moscow, 1966, 532 p. (in Russian).
[35] Yu.G. Chukalkin, V.R. Shtirts, B.N. Goshchitskii, Phys. Status Solidi (a) 112 (1989) 161.
[36] A.C. Wright, J. Non-Cryst. Sol. 40 (1980) 325.